

Sunspot simulations with MURaM

I. Parameter study using potential field initial conditions

Markus Schmassmann¹, Nazaret Bello González¹, Rolf Schlichenmaier¹, Jan Jurčák²

¹ Institut für Sonnenphysik (KIS), Georges-Köhler-Allee 401a, 79110 Freiburg, Germany, e-mail: {schmassmann, nbello, schliche}@leibniz-kis.de

² Astronomical Institute of the Czech Academy of Sciences, Fričova 298, 25165 Ondřejov, Czech Republic, e-mail: jurcak@asu.cas.cz

Received 24 December 2025 / Accepted xx Yyyyyy 2026

ABSTRACT

Context. Existing sunspot simulations fail to reproduce the observed magnetic field distribution due to an artificially increased horizontal magnetic field component at the upper boundary.

Aims. We explore alternative ways to better reproduce the magnetic and dynamic properties of observed sunspots.

Methods. We use the MURaM radiative MHD code. As initial conditions, we placed a potential magnetic field into small-scale dynamo simulations and used potential field extrapolation as top boundary conditions.

Results. We find that: (1) Simulations with increasing initial magnetic field strengths (20 kG, 40 kG, 80 kG, and 160 kG) show increasing spot, umbral, and penumbral sizes. (2) The penumbral-to-spot sizes are smaller than those measured in the observed sunspots. (3) In none of the runs are pure Evershed (radially outwards) flows. Instead, bi-directional flows with inflows in the inner penumbra and outflows in the outer penumbra were measured similarly to observations of early stages of penumbra formation for runs with 80 kG or more and 96/32 km resolution, whereas runs with 40 kG or less showed pure inflows. (4) Simulations with 160 kG and an increased resolution of 32/16 km contain filaments with bi-directional and Evershed flows. (5) Simulations with fluxes $> 10^{22}$ Mx show unrealistically strong fields in the umbra. (6) The best runs with 160 kG and 10^{22} Mx give realistic profiles of B_z and B_r with radius, although stronger fields than observed. (7) Increasing the width of the box and reducing the overall flux by subtracting a uniform opposing vertical field have little influence on the internal spot dynamics and fields. Still, it changes the average vertical field outside the spot.

Conclusions. Simulations of small (10^{22} Mx) sunspots with an initial potential field and intensified magnetic field strength at the bottom of the box seem to best reproduce observations of the initial stages of sunspot formation. Our findings also suggest that increased numerical resolution may be critical for achieving fully developed penumbrae.

Key words. Sun: photosphere – Sun: magnetic fields – sunspots – Magnetohydrodynamics (MHD) – Methods: numerical

1. Introduction

The art of MHD sunspot simulations has developed only recently. In 2007, Heinemann et al. (2007) presented the first slab simulation of a sunspot, followed by similar simulations by Scharmer et al. (2008) and Rempel et al. (2009b). These simulations provided the first insights into the penumbral fine structure. After initial trials, particularly in (Rempel et al. 2009a), Rempel (2012) managed to run MHD simulations of a circular sunspot that qualitatively reproduced the observed properties of penumbral fine structure. In other words, the structure of the penumbral filaments is comparable to the observational analysis of (Tiwari et al. 2013).

However, the formation of an extended penumbra is achieved in these MHD simulations by imposing artificial top boundary conditions that make the magnetic field more horizontal at the photospheric level. As shown by (Jurčák et al. 2020), the global magnetic properties of the resulting sunspot are not fully realistic. The magnetic field inclination on the umbral/penumbral boundary is around 60° , which is significantly more horizontal than in the observed sunspots, where the largest values of inclination are around 45° and those are found only in large sunspots with more flux than the simulated sunspot. Further-

more, the vertical magnetic field component, B_z , at the umbral boundary in these simulations is below the value expected from observations, a B_z^{stable} of around 1.8 kG. In Jurčák et al. (2020), it was also shown that the inclination distribution as a function of the fractional spot radius as well as B_z at the umbral boundary of observed sunspots, is comparable to an MHD simulation of a sunspot with a potential field as an initial condition. The use of a potential field as an initial condition for sunspot simulations was first proposed by Nordlund (2015), who used slab geometry. Based on this idea, we performed an MHD simulation of a circular sunspot, as described by Jurčák et al. (2020). To find the best agreement between the simulated and observed sunspots, we conducted a parameter study of sunspot simulations using potential field initial conditions.

The sunspot simulations of Panja et al. (2021) also use potential top boundary conditions. However, the penumbra of their sunspots is wide only between the nearby opposite polarity spots, and very narrow in the perpendicular direction. Furthermore, their simulations are, by design, strongly affected by fluting instability, which makes them short-lived. The same authors also created simulations of starspots on other main-sequence stars (Panja et al. 2020).

Table 1. Simulation parameters.

Sunspot run	B_0 [kG]	B_{opp} [G]	F_{Gauss} [10^{22} Mx]	F_{tot} [10^{22} Mx]	Box width [Mm]	d_h [km]	Run time [h]	t_{ref} [h]
20_opp000o	20.0	0	1	1	49.152	96	7.2038	2.8847 – 4.0839
40_opp000o	40.0	0	1	1	49.152	96	7.1966	2.8815 – 4.0789
80_opp000o	80.0	0	1	1	49.152	96	7.2167	2.8889 – 4.0911
160_opp000o	160.0	0	1	1	49.152	96	14.429	2.8886 – 4.0908
160_opp000ho	160.0	0	1	1	49.152	32	7.7131	7.2163 – 7.7131
160_opp000h	160.0	0	1	1	49.152	32	7.9997	3.0149 – 4.0149
160_opp050c	160.0	50	1.120796	1	49.152	96	4.0205	3.0142 – 4.0205
160_opp100c	160.0	100	1.241592	1	49.152	96	4.0075	3.0075 – 4.0075
160_opp150c	160.0	150	1.362388	1	49.152	96	4.0076	3.0076 – 4.0076
160_opp200c	160.0	200	1.483184	1	49.152	96	4.0057	3.0057 – 4.0057
160_opp300c	160.0	300	1.724776	1	49.152	96	4.0045	3.0045 – 4.0045
160_opp000	160.0	0	1	1	49.152	96	40.025	3.0111 – 4.0147
160_opp050	160.0	50	1	0.879204	49.152	96	4.0226	3.0182 – 4.0226
160_opp100	160.0	100	1	0.758408	49.152	96	4.0367	3.0167 – 4.0367
160_opp150	160.0	150	1	0.637612	49.152	96	4.0135	3.0123 – 4.0135
160_opp200	160.0	200	1	0.516816	49.152	96	4.0400	3.0223 – 4.0400
160_opp300	160.0	300	1	0.275224	49.152	96	4.0313	3.0198 – 4.0313
160_opp100w	160.0	100	1	0.033632	98.304	96	4.0267	3.0199 – 4.0267
160_opp150w	160.0	150	1	-0.449552	98.304	96	4.0156	3.0156 – 4.0156
160_opp200w	160.0	200	1	-0.932736	98.304	96	4.0214	3.0138 – 4.0214
160_opp000b	160.0	0	1	1	49.152	96	6.1536	2.9848 – 4.0010
alpha1.0	6.4		1.198126	49.152	32	6.5096	6.0096 – 6.5096	
alpha1.5	6.4		1.198126	49.152	32	6.4120	5.9120 – 6.4120	
alpha2.0	6.4		1.198126	49.152	32	6.4133	5.9133 – 6.4133	
alpha2.5	6.4		1.198126	49.152	32	6.4222	5.9222 – 6.4222	
NOAA AR 11591					362.5		2012.10.18 10:00:00	

Bhatia et al. (2025) simulates starspots, extending (Panja et al. 2020), but again forcing the magnetic field at the top to be inclined, resulting in too horizontal fields, at least when comparing the G2V starspot to sunspot observations.

Hideyuki Hotta investigated the effect of higher resolution on sunspot simulations with a potential-field top boundary condition. Matthias Rempel joined this investigation and also analysed what happens when the resolution is changed during the simulation runs. All simulations in their investigation use potential field top boundary conditions. While presentations of preliminary analysis (Rempel & Hotta 2025) are very encouraging, these results have not yet been published in a peer-reviewed journal. Furthermore, the high resolution used in these simulations results in prohibitively high costs.

In solar observations, the penumbra forms around existing flux concentrations (e.g. Schlichenmaier et al. 2010b). Various authors have done flux emergence simulations (e.g. Cheung et al. 2010; Chen et al. 2017; Hotta & Iijima 2020). These simulations show, consistent with solar surface observations, that deeply anchored bundles rise coherently up to around 2 Mm below the surface, to then decay in small parts that rise with individual convective cells, and at the surface re-coalesce to larger structures that end up forming sunspots (see *tethered-balloon* model of Spruit 1981). However, they either manage to create a wide enough penumbra at most in some directions, or have incorrect flow directions (in-flows along the filaments and down-flows at the umbral boundary) in most or all penumbral filaments.

In the following, Sec. 2 describes the simulation setups, including the initial conditions, their variables, and the values they take, as well as the data processing methods. Section 3 presents the results, focusing on intensities, surface flows, and magnetic

field properties. Section 4 provides a summary and conclusion, including a discussion of how the results relate to observations.

2. Simulation setups and processing

Our simulations were run using the MPS/University of Chicago Radiative Magneto-hydrodynamics code (MURaM; Vögler et al. 2004; Rempel et al. 2009b). We use the updated numerical treatment from Rempel (2017), without using the coronal features introduced therein. The bottom boundary is open to mass flows, and the magnetic fields are extrapolated symmetrically, as described by Rempel (2014, Sec. 2.2, item 'OSb'). The top boundary is open to inflows, closed to outflows, and there, the magnetic field is potential as in Cheung (2006, Appendix C.1) and Rempel (2012, Appendix B).

2.1. Initial condition: Potential with opposing flux

The initial vertical component of the magnetic field at the bottom of the box is given by

$$B_{z,0}(r) = B_0 \exp\left(-\frac{r^2 B_0 \pi}{F_{\text{Gauss}}}\right) - B_{\text{opp}}, \quad (1)$$

whereby B_0 is the initial maximal magnetic field, r is the distance from the spot axis, and F_{Gauss} is the flux contributed by the Gaussian distribution. An alternative to a pure Gaussian is the subtraction of a uniform vertical magnetic field, B_{opp} . Integrating horizontally gives the total flux through the box

$$F_{\text{tot}} = \int B_{z,0} \left(\sqrt{x^2 + y^2} \right) dx dy = F_{\text{Gauss}} - B_{\text{opp}} w^2, \quad (2)$$

Table 2. Simulation results.

Sunspot run	r_u [Mm]	r_s [Mm]	r_{pu}/r_s	F_{spot} [10^{22} Mx]	$d_t F/F$ [%/h]	$\max B_z$ [G]	$\max B_r$ [G]	$r_{\max B_r}$ [Mm]	$\min v_z$ [km/s]	$r_{\min v_z}$ [Mm]	$\min v_r$ [km/s]	$r_{\min v_r}$ [Mm]	$\max v_r$ [km/s]	$r_{\max v_r}$ [Mm]
20_opp000o	7.484	10.546	0.290	0.680	1.156	4275.1	2247.0	7.488	-1.261	8.35	-3.598	8.74	0.606	17.57
40_opp000o	6.975	11.029	0.368	0.676	3.655	5424.2	2213.2	5.376	-1.076	7.49	-2.662	8.16	0.676	14.30
80_opp000o	6.723	11.508	0.417	0.628	4.420	5833.2	2154.4	5.376	-0.558	7.58	-0.793	7.10	2.339	12.19
160_opp000o	6.236	12.329	0.494	0.631	11.668	4346.9	2096.7	5.760	-0.771	7.01	-0.903	7.01	3.314	12.29
160_opp000ho	7.454	12.854	0.420	0.779	1.683	4518.3	2026.2	6.368			-0.302	6.14	2.469	13.38
160_opp000h	5.956	12.529	0.525	0.598	5.641	5360.4	2194.3	4.960	-0.366	5.41	-0.408	5.41	4.297	14.91
160_opp050c	7.221	13.329	0.458	0.703	12.148	4838.8	2349.8	4.992	-0.575	7.10	-0.560	7.10	3.476	14.02
160_opp100c	7.355	14.001	0.475	0.764	11.258	5239.6	2538.5	6.144	-0.562	7.39	-0.632	5.38	3.357	13.44
160_opp150c	7.670	14.527	0.472	0.837	9.408	5652.8	2737.0	5.280	-0.563	8.74	-0.872	6.82	3.826	14.69
160_opp200c	8.058	15.125	0.467	0.916	10.771	5924.1	2893.7	6.144	-0.691	6.43	-1.266	6.91	3.630	15.17
160_opp300c	8.658	15.939	0.457	1.081	11.502	6607.6	3084.6	6.240	-0.566	7.10	-0.988	7.20	3.719	18.72
160_opp000	6.789	12.975	0.477	0.648	8.468	4464.8	2166.0	5.856	-0.578	6.24	-0.740	6.24	3.045	14.59
160_opp050	6.848	12.891	0.469	0.630	10.494	4478.0	2142.3	5.952	-0.463	6.24	-0.422	6.34	3.086	14.50
160_opp100	6.776	12.861	0.473	0.608	10.745	4435.4	2261.7	5.760	-0.589	7.30	-0.895	6.62	3.709	13.25
160_opp150	6.790	13.001	0.477	0.593	12.061	4380.4	2212.5	5.664	-0.598	6.14	-0.932	6.72	3.694	12.67
160_opp200	6.638	12.921	0.486	0.577	10.392	4475.4	2199.3	5.952	-0.724	6.53	-1.168	6.53	3.625	12.77
160_opp300	6.758	12.877	0.475	0.567	12.328	4360.5	2208.2	5.856	-0.574	6.43	-0.656	6.43	3.897	12.58
160_opp100w	6.633	13.052	0.491	0.577	11.040	4239.6	2081.8	6.144	-0.581	7.01	-0.708	6.24	3.601	14.88
160_opp150w	6.487	13.312	0.512	0.569	12.343	4241.1	2095.3	4.704	-0.545	6.72	-0.399	6.62	3.321	14.40
160_opp200w	6.606	13.307	0.503	0.553	12.981	4282.6	2163.9	5.376	-0.494	6.53	-0.516	5.66	3.757	13.15
160_opp000b	8.498	11.659	0.271	0.709	4.715	4543.3	1611.7	7.296	-1.001	9.89	-1.524	10.37	0.657	16.80
alpha1.0	10.698	13.937	0.232	1.059	-4.309	3641.2	1597.5	9.632					1.050	11.26
alpha1.5	10.722	15.080	0.289	1.031	-5.540	3877.7	2248.9	9.504					3.985	13.34
alpha2.0	10.881	16.482	0.340	1.015	-5.873	4180.3	2379.9	9.504					4.130	14.40
alpha2.5	10.971	17.288	0.365	1.012	-5.765	3359.9	2548.9	9.152					4.380	14.43
NOAA AR 11591	6.326	14.397	0.561	0.548		2829.2	1402.0	6.888						

whereby w is the width of the box in both the horizontal directions. This value is the same for all heights and all times (but not over the $\tau = 1$ iso-surface). The initial field throughout the box is given by potential field extrapolation according to

$$B_z = \mathcal{F}^{-1} \left(\mathcal{F}(B_{z,0}) e^{-z|k|} \right) \text{ and } B_x = \mathcal{F}^{-1} \left(\mathcal{F}(B_{z,0}) \frac{-ik_x}{|k|} e^{-z|k|} \right) \quad (3)$$

whereby \mathcal{F} represents the horizontal Fourier transform. B_y can be obtained by replacing k_x by k_y , or in our axi-symmetric case, by $B_y(x, y) = B_x(y, x)$. This extrapolation is the same as the top boundary condition mentioned above, with the difference that there $z = 0$ stands for the top (extrapolation into the ghost cells during the simulation run) instead of the bottom of the box (creating the initial field).

The potential extrapolation results in the initial B_z falling much more slowly with increasing radius outside the spot (see Fig. A.1, top-left panel) than self-similar initial conditions as in Rempel (2012). For all initial conditions with a pure Gaussian in the smaller simulation box, B_z remained above 155 G everywhere in the box. Given that in observations, B_z outside the spot vanishes, we tested the effect of subtracting a uniform vertical field (B_{opp}). This subtraction can be performed before or after extrapolation, and the result is the same.

2.2. Simulation dataset

The simulation runs described in this article are listed in Table 1, whereby the following parameters were varied:

- Initial maximal magnetic field strength B_0 : 20 kG, 40 kG, 80 kG, or 160 kG (most runs). B_0 is the first number in run names.¹
- Box width, w : 49.152 Mm (most runs) or 98.304 Mm. Runs with $w = 98.304$ Mm have names ending in 'w'.
- $F_{\text{Gauss}} = 10^{22}$ Mx (most runs) or $F_{\text{tot}} = 10^{22}$ Mx. Runs with $F_{\text{Gauss}} > 10^{22}$ Mx have names ending in 'c'.
- Opposing magnetic field B_{opp} : 0 G, 50 G, 100 G, 150 G, 200 G and 300 G. This is the second number in the simulation names.
- Most runs use a 96 (32) km horizontal (vertical) resolution, except the high-resolution runs with 32 (16) km, which have a name ending containing 'h'. All low-resolution simulations used grey radiative transfer.

The simulations with names ending in 'o' were run with a previous version of the MURaM code and provided bolometric intensities instead of 500 nm continuum intensities, and contain further subtle differences that we will discuss later, where necessary.

The box was 8.192 Mm deep for all our simulations, but we provided comparison simulations 'alpha*', which were only 6.114 Mm deep. These are continuations of those started in Rempel (2012), which were described in Jurčák et al. (2020) as 'type II'. They have self-similar initial conditions and top boundary conditions, which force the field to be more horizontal by a factor of α than a potentially extrapolated field.

While the simulation '160_opp000o' continued running at low resolution, after 4.8121 h it was regridded to the higher 32 (16) km resolution, and at time 7.2163 h switched over

¹ These unphysically strong initial fields at the bottom of the box get quickly reduced by an initial transient.

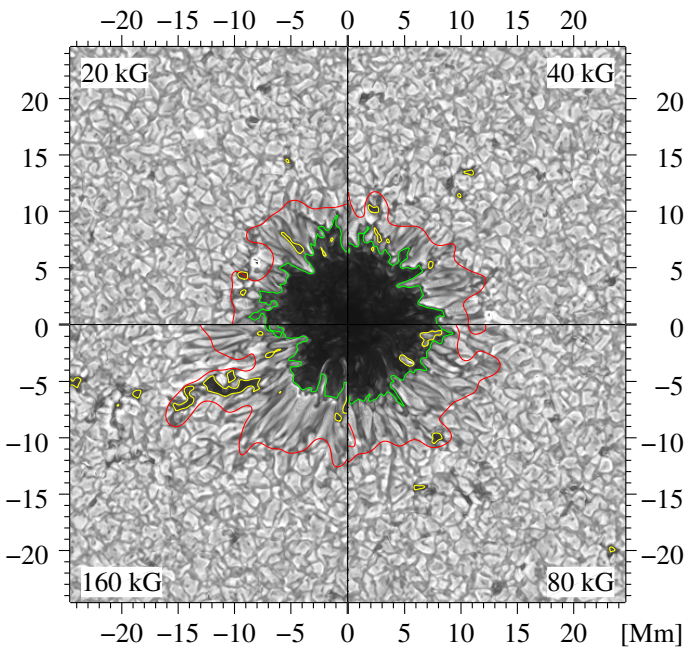


Fig. 1. Quadrants of bolometric intensity maps for four selected simulation runs with different initial magnetic field strengths. From top-left clock-wise: $B_0 = 20$ kG, 40 kG, 80 kG and 160 kG. The magnetic flux is the same for all four runs: $F = 10^{22}$ Mx.

to non-grey radiative transfer. In that form, which we name '160_opp000ho', it was described as 'type I' in Jurčák et al. (2020). Simulation '160_opp000h' was run in the higher resolution from the start.

All high-resolution simulations presented here (160_opp000{h,ho}', 'alpha*') use non-grey radiative transfer (Nordlund 1982; Ludwig 1992; Vögler et al. 2004) with four opacity bins. The main benefit of this is that it allows forward radiative transfer, degradation to instrumental resolution, adding noise, and subsequent inversions, as done in Jurčák et al. (2020).

The simulation '160_opp000b' suppresses mass flows through the bottom in regions where $|B_z| \gtrsim 10$ kG.

The azimuthal averages of the initial conditions at photospheric heights are shown in Fig. A.1.

In addition, we used the Helioseismic and Magnetic Imager (HMI/SDO) (Scherrer et al. 2012) observations of NOAA AR 11591 for comparison. For more details on this spot, in particular its umbral and spot boundary, see Schmässmann et al. (2018, 2025).

2.3. Data processing

During the simulation run, every 50 time steps, the intensity, I_c , as well as velocities, v_{xyz} , and magnetic field vectors, B_{xyz} , at the location of the $\tau = 1$ layer were saved. This corresponds to one slice every ≈ 36 s or ≈ 43 s. The larger time steps are for the older simulations (with names ending on 'o'), where the Alfvén speed limiter was set to a lower value. For every simulation, we evaluated 101 such slices, thus covering ≈ 1 h or ≈ 1.2 h. The time ranges covered are listed as t_{ref} in Table 1. The different Alfvén speed limiter values only change the length of the computation time steps and affect the low-density regions above the umbra, which are not relevant to this study.

The quiet Sun intensity I_{qs} , as well as the umbral and spot boundaries, were calculated using the same methods as in Schmässmann et al. (2021), where the umbral boundary corre-

sponds to $I_c = 0.5I_{qs}$ and the spot boundary to $I_c = 0.9I_{qs}$. For consistency, we calculated a single I_{qs} for all new simulations (not ending on 'o') by averaging over the quiet Sun data of all simulations and all time steps, and separately the same for the old simulations (with names ending on 'o'). These two sets of simulations were treated separately because the changes in MURaM between these runs resulted in incompatible intensity values (500nm continuum vs. bolometric). Studying maps of intensity and velocities shows that the umbral boundary is sharp and well retrieved by this procedure, whereas an accurate determination of the spot boundary would require identifying individual convective cells and classifying them as belonging to the spot or quiet Sun. Using a contour on a degraded intensity map, as we do, will only result in an approximate result, but it is good enough to retrieve the spot areas and radii.

In the next step, the vectors were transformed to obtain the radial field², B_r , total field, $|B|$, inclination to the surface normal $\gamma = \arctan(\sqrt{B_x^2 + B_y^2}/B_z)$ and correspondingly for velocities. The values were then remapped from Cartesian to cylindrical coordinates, after which an azimuthal average was performed. In addition to the averages of the values themselves (e.g. mean vertical velocity, v_z), the fraction of positive terms (upflow filling factor $n_{v_z>0}$) and signed averages (mean upflow velocity $v_{z,+}$, mean downflow velocity $v_{z,-}$) were calculated.

In the final step, we performed a least-squares linear fit of all time-dependent parameters, including the azimuthal averages. Then we evaluate the value of this linear function at 4 h ('160_opp000ho': 7.5 h, 'alpha*': 6.3 h). For simplicity, hereafter in this article, these temporal fits are implied unless mentioned otherwise. For instance, when we refer to azimuthal averages, we mean these values of the linear functions at 4 h fit to the azimuthal averages. Where we show maps, we use those of the last time in the reference range (last column of Table 1).

3. Results

3.1. Intensity

Figure 1 shows the bolometric intensity maps of sunspot simulations with four values of the initial maximal magnetic field strength B_0 : 20 kG, 40 kG, 80 kG, and 160 kG, respectively. All runs contain the same flux (10^{22} Mx), no opposing field B_{opp} and are in the small (49 Mm wide) box. The green line shows the umbral boundary as the longest contour of $I = 0.5I_{qs}$, in yellow other contours at the same intensity level, and in red the spot boundary as the longest contour at $I_c = 0.9I_{qs}$. The other contours at this level are not shown.

As a global property, the size of the penumbral increased with increasing initial magnetic field strengths, B_0 , up to 160 kG. Simulation runs with $B_0 = 20$ kG and 40 kG show elongated convective cells resembling penumbral filaments. The $B_0 = 160$ kG run shows the slenderest and longest penumbral filaments, and $B_0 = 80$ kG shows an intermediate state.

Figure 2 and the bottom right panel of Fig. 4 shows the azimuthal averages of the intensity for selected simulations. The vertical dashed lines show the average spot and umbral radii, r , calculated from the contour areas using $r = \sqrt{A/\pi}$. For all simulations, the umbral and spot sizes, and their penumbral fractions are given in Table 2, columns r_u , r_s , and $r_{pu}/r_s = 1 - r_u/r_s$. Increasing F_{Gauss} beyond 10^{22} Mx increases the sizes of the umbrae and spots. Based on sunspot statistics, Kiess et al. (2014a)

² Radial in sunspot simulations refers to a cylindrical coordinate system, with z aligned with the spot axis and increasing with height.

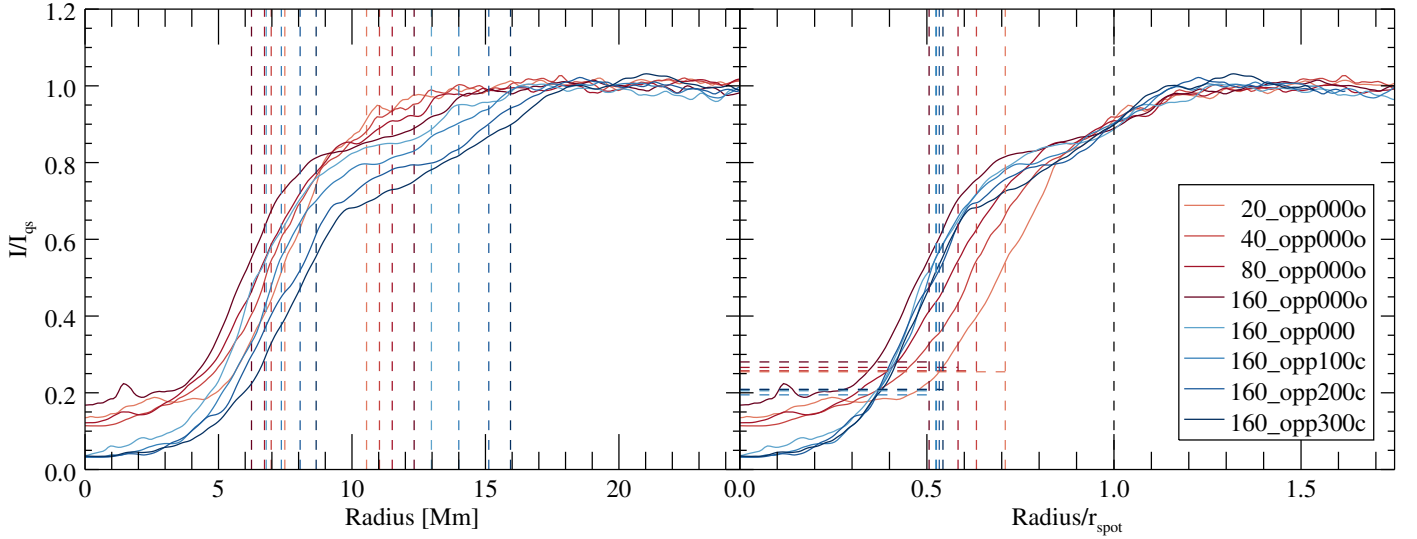


Fig. 2. Azimuthally averaged intensity I/I_{qs} (solid lines) as a function of radius in Mm and fraction of the spot radius. The colours indicate the simulations listed in the inset legend. For the older runs (with names ending with 'o', red), the bolometric intensity is shown, and for the other runs (blue), the continuum intensity is shown. Vertical dashed lines show the position of the umbral (left panel with $R < 10$ Mm, right panel $R < 1$) and spot boundaries (left panel $R > 10$ Mm, right panel $R = 1$ black). The horizontal dashed lines in the right panel show the average umbral intensity. Values corresponding to the location of the vertical dashed lines are given in Table 2, columns r_u , r_s , $r_{u/s}$.

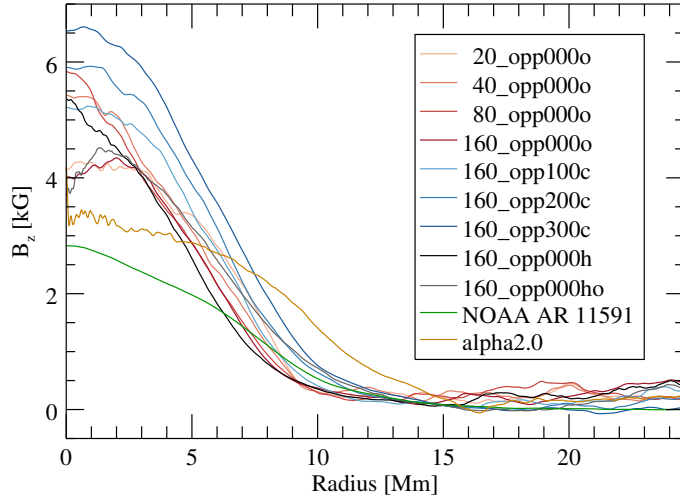


Fig. 3. Vertical magnetic field component, B_z , of selected simulations. B_z from an observation (green) is also displayed for comparison.

showed that the umbral radii increase linearly with the spot flux. In our simulations, the umbral radii increased with spot flux, consistent with their linear fit. However, for $B_0 < 160$ kG, the penumbral fractions are smaller than for those with $B_0 = 160$ kG, which, at 47%–52%, are already below the typical value observed in sunspots, where the penumbra covers about 60% of the spot size (e.g., Keppens & Martínez Pillet 1996; Westendorp Plaza et al. 2001; Mathew et al. 2003; Borrero et al. 2004; Bellot Rubio et al. 2004; Sánchez Cuberes et al. 2005; Beck 2008; Borrero & Ichimoto 2011; Chowdhury et al. 2024, and references therein). In summary, our simulations provide sunspots with a realistic umbral size but diminished penumbral length; that is, our simulations provide smaller sunspots than the observed stable ones. However, the simulated spot sizes resemble those of developing sunspots during penumbra formation (see, e.g. Jurčák et al. 2014).

The difference in brightness in the umbrae between older runs (names ending with 'o', red lines in Figs. 2) and the newer ones (blue lines) are caused by the former giving bolometric intensities, $I = I_{bol}$, whereas the latter are giving the continuum intensity at 500 nm, $I = I_{c500}$. The differences between these intensities are consistent with the expectations of blackbody radiation.

3.2. Surface magnetic fields

In Fig. 3 we plot the radial dependence of the azimuthally averaged B_z for the runs given in the figure's legend. Simulations with $F_{Gauss} > 10^{22}$ Mx (names ending in 'c') have stronger vertical magnetic fields in the spot axis $B_z(r = 0)$ at the average $\tau = 1$ height in the initial condition (see top left panel of Fig. A.1, three light blue lines) than those with $F_{Gauss} = 10^{22}$ Mx (dark blue line). This results in unrealistically strong fields in the later stages of the simulation (see Fig. 3, blue lines, and the 'max B_z ' column in Table 2). By unrealistic, we mean stronger than observed on the sun in spots of comparable fluxes (Rezaei et al. 2012; Kiess et al. 2014b).

The initial phase of the simulations had both concentrating and dispersing effects in the magnetic fields at the spot centre. For the $B_0 = 160$ kG simulations starting with the lower resolution (96/32 km), the concentrating effects are slightly stronger than the dispersing effects, resulting in a moderate increase in B_z . For the simulation starting with a higher resolution ('160_opp000h'), the concentrating effects were stronger, resulting in an excessively high B_z . For $B_0 = 40$ kG and 80 kG, the dispersing effects are weaker than those for the $B_0 = 160$ kG simulations, resulting in too strong max B_z . This is consistent with a simulation with $B_0 = 160$ kG, but with a closed bottom boundary at the spot foot-point ('160_opp000b'), which also lacks the very dynamic initial phase with its dispersion effects and has a higher max B_z . The simulation with a closed bottom boundary also lacked a properly formed penumbra, and the few elongated granules had in-flows along the full length and down-flows outside the umbral boundary.

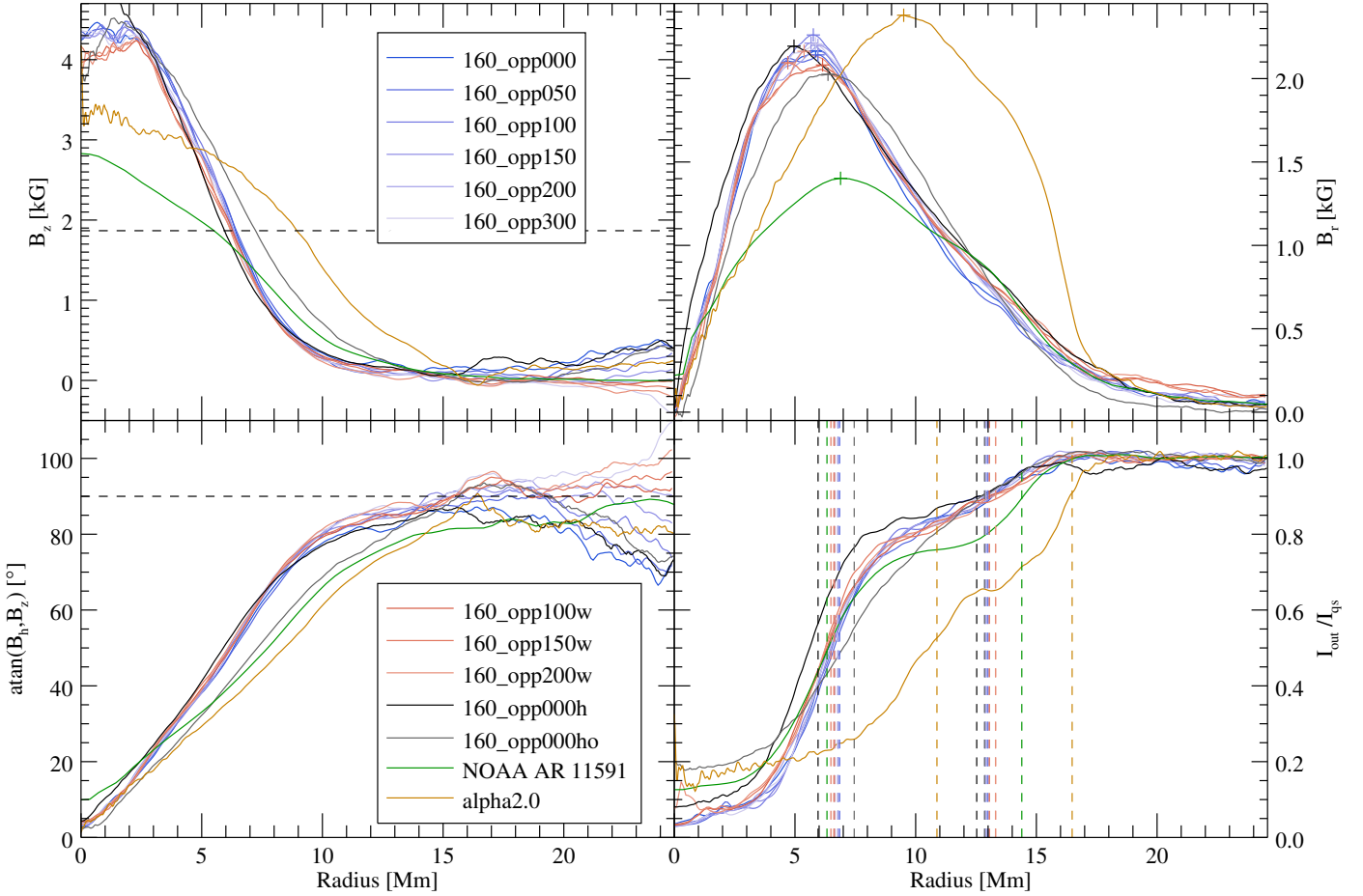


Fig. 4. Azimuthal averages of the vertical magnetic field component, B_z (top left), the radial magnetic field component, B_r (top right), the inclination (bottom left), and the intensity, I_{out} (bottom right), of our more realistic simulations (blue, red, black and grey), and of an observation (green), and an old reference simulation (gold). Horizontal dashed lines refer to $B_z = 1867$ G, the observed critical value for penumbral-type convection to operate (top left), and to an inclination of 90° , meaning a horizontal field (bottom left).

Low-resolution simulations with $F_{\text{Gauss}} = 10^{22}$ Mx and $B_0 = 160$ kG have max $B_z = 4240$ – 4478 G, and B_z drops with increasing radius to values of 200 G similar for all such simulations. Outside the spot, the values for B_z fluctuate, whereas simulations in larger boxes or higher B_{opp} fluctuate around lower values, as shown in the top left panel of Fig. 4.

Simulations with $F_{\text{Gauss}} > 10^{22}$ Mx have increased B_r compared to those with $F_{\text{Gauss}} = 10^{22}$ Mx. Beyond that, within the spot, all simulations with $B_0 = 160$ kG have a similar dependence of B_r on the fractional spot radius, as depicted in the upper right panel of Fig. 4. The $B_0 = 20$ kG simulation has the maximum B_r at a larger radius, consistent with the higher umbral fraction. All $B_0 < 160$ kG simulations have a faster drop of B_r outside the spot than the $B_0 = 160$ kG simulations. Of the $B_0 = 160$ kG simulations, B_r decreases more slowly outside the spot for those in larger boxes, indicating that the drop-off of B_r in smaller boxes may be caused by the horizontal periodic boundary conditions.

The increase in field inclination, γ , with fractional spot radius up to 80° is similar for all $B_0 = 160$ kG simulations (Fig. 4, bottom left panel), and γ rises more slowly with the fractional spot radius for the $B_0 < 160$ kG simulations, which is consistent with their larger umbral fraction. The other differences in the initial conditions are shown in the bottom right panel of Fig. A.1 within the spot were removed during the dynamic ini-

tial phase. Outside the spot, the average inclination fluctuated around 75° – 105° , depending on the average B_z there.

3.3. Surface flows

The simulations with $B_0 = 20$ kG and 40 kG have inflows toward the umbra along the full length of all elongated convective cells, with downflows at umbral boundaries. As this is not consistent with what is observed on the sun, we do not perform a more detailed discussion of the surface flows in these simulation runs. A comparison of the other runs with observations is done in Sect. 4.

The simulations with $B_0 = 80$ kG and 160 kG and low resolution (96/32 km) have strong in- and down-flows in most umbral ends of penumbral filaments (filament heads), with out- and up-flows in the middle and outer parts of the filaments. Down-flows were also observed between the filaments and at the outer ends. An example map of the radial flows (in- and out-flows) and vertical flows (up and down) is presented in Fig. 5.

In the umbra, the dominant contribution to the vertical flows, v_z , is an overall oscillation, which at the time shown here is near a zero crossing, and hence not visible in the map. Our azimuthally averaged and temporally fitted values of v_z have these oscillations averaged out over time. This was verified in some simulations by subtracting the $\tau = 1$ surface oscillations from the vertical velocities. Outside the umbra, the averages of the up-flow filling factor and separate averages over up- and down-flow

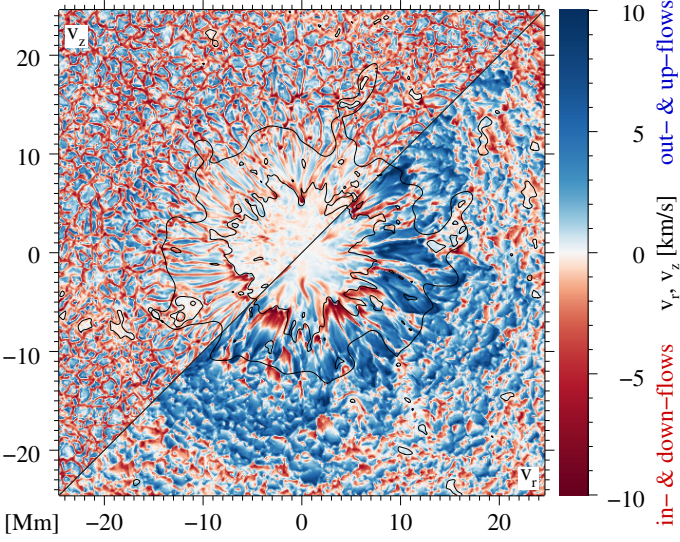


Fig. 5. Surface velocity map of sunspot run '160_opp000'. Upper left: Vertical flows, v_z , downflows in red, upflows in blue. Lower right: Radial velocities, v_r , inflows red (towards the spot centre), outflows blue. The black contours are the same as shown in Fig. 1.

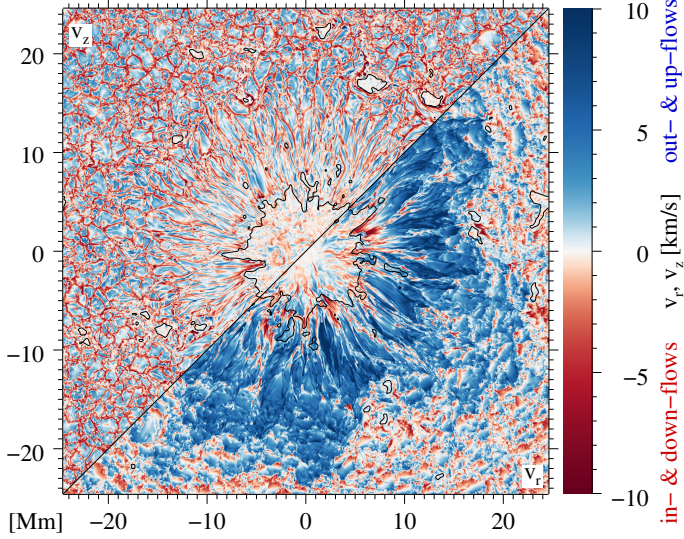


Fig. 6. As Fig. 5, but for sunspot run '160_opp000h' (high resolution). No spot boundary contour.

speeds change quantitatively, but the radial distance of the minima and maxima is not affected. Inside the umbra, these values are not usable because vertical oscillations are the dominant contributors to the velocity.

The following discussion focuses on the common flow behaviour of the $B_0 = 160$ kG simulations. We find that the simulation run with $B_0 = 80$ kG is similar in many aspects, but the shorter penumbral filaments result in slower outflows.

In terms of azimuthal averages, the outflow speed $v_{r,+}$ increases with increasing radius until the spot boundary, and then slowly decreases. Inflow speeds $-v_{r,-}$ increased until the umbral boundary, then converged to the lower quiet sun value. The outflow filling factor $n_{v_r>0}$ has values of 39–48% at a local minimum near the umbral boundary, then rapidly increases and tapers off to a maximum around the spot boundary of 88–93% for the $B_0 = 160$ kG simulations. This results in the radial velocity, v_r , having a minimum near the umbral boundary and a maxi-

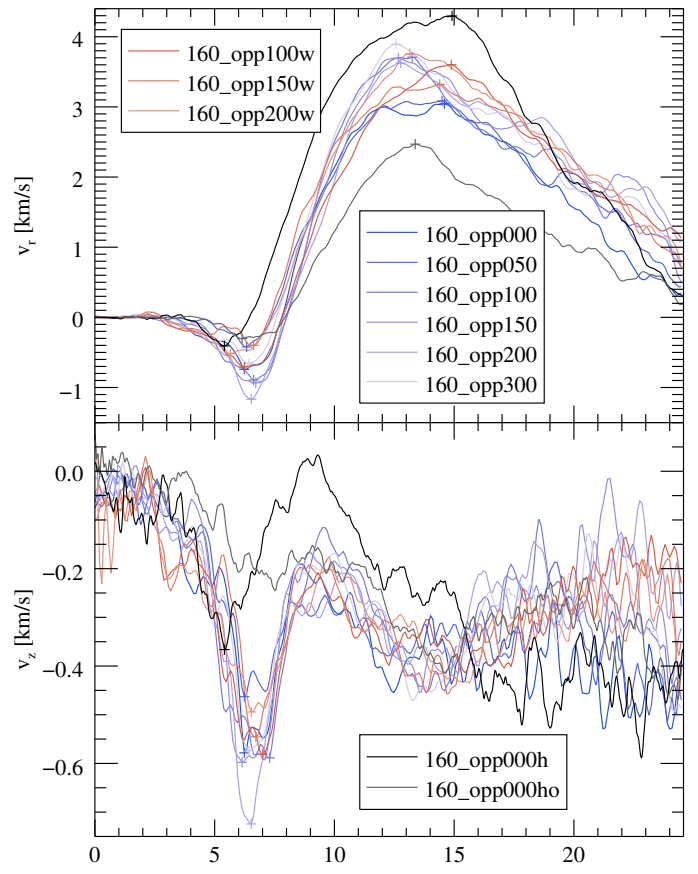


Fig. 7. Azimuthally averaged radial, v_r (top panel), and vertical, v_z (bottom panel), velocities of our more realistic simulations

mum near the spot boundary. The minima, maxima, and their locations of our simulation runs are listed in Table 2, and v_r and v_z are shown in Fig. 7, where the extrema are marked with + symbols.

Up-flow speeds $v_{z,+}$ increased steadily with radius until they reached the quiet-sun average at around $1.2 r_s$. Down-flow speeds $-v_{z,-}$ have a local speed maximum near the umbral boundary, then the speed decreases over the inner penumbra to increase to the quiet Sun average. Outside the umbral boundary, the up-flow filling factor $n_{v_z>0}$ increased over the same range as the down-flows get slower with increasing radius. Outside this narrow range, any trend in the radial dependence of the filling factor is sufficiently weak to be hidden by random-looking fluctuations. The lower panel of ('160_opp000h') shows that inside the central umbra, vertical velocities v_z are on average near zero, then drop to a local minimum near the umbral boundary, followed by a quick increase over the inner part of the penumbra, and a decrease to the quiet sun average over the width of the rest of the penumbra, accompanied by an increase in fluctuations.

Having a negative average quiet-sun vertical velocity is not a contradiction to the convective blue shift, as that is caused by weighting the average of the light, meaning that the bright granular up-flows outshine the darker inter-granular down-flows. Our average is negative because the $\tau = 1$ surface in the inter-granular lanes is lower; hence, the down-flows are faster than the up-flows.

The maximal total velocity, v , was found outside but near the spot boundary, outside of which it dropped to the quiet-sun

average. Most simulation runs have a minor local maximum near the umbral boundary.

In summary, as shown in Fig. 5, a pattern that appears characteristic of the potential field simulations with $B_0 \geq 80$ kG presented here is the bi-directional flows exhibited by the penumbral structure: radial outflows (blue) resembling the observed Evershed flows are present in the mid and outer-penumbra, yet the inner penumbra is characterised by strong inflows (red) combined with down-flows. Bi-directional flows were first reported in high-resolution observations by Schlichenmaier et al. (2011) as counter-Evershed flows. Recently, García-Rivas et al. (2024) showed that some of these counter-Evershed flows correspond to bi-directional flows that act as a precursor to the formation of a stable penumbra.

The simulation with a closed bottom boundary inside the magnetic trunk ('160_opp000b') has elongated granules instead of penumbral filaments, hence no outflows.

Figure 6 shows that the high-resolution (32/16 km) simulations have, however, both filaments with bi-directional flows and those with normal Evershed flows, meaning up-flows in the filament heads, outflows along the whole lengths of the filaments, and down-flows at the outer ends and between the filaments. The simulation that started with high-resolution ('160_opp000h') has faster outflows (Fig. 7, upper panel), consistent with the resolution dependence of the Evershed flow speed reported by Rempel (2012). The simulation that started at low resolution and was later regridded to high resolution ('160_opp000ho') has slower outflows, because the flow speeds decrease over time, and this simulation is evaluated at a later time.

3.4. Flux emergence

Our low-resolution (96/32 km) simulations with $B_0 = 160$ kG and open bottom boundary (names starting with '160' and ending containing neither 'h' nor 'b') keep increasing their flux during our observation time (Table 2, column $d_t F/F$, 8.5–13.0%/h). This corresponds to flux emergence. In the only simulation run for substantially longer than 4 h ('160_opp000'), the stalling of flux emergence at 8–10 h coincides with a narrowing of the penumbra and the disappearance of most outflows.

In simulation '160_opp000ho', for which the data is evaluated 3.5 h later than in most other simulations, flux emergence is tailing off. In the simulation with a closed bottom boundary inside the magnetic trunk ('160_opp000b'), only little flux emergence is observed.

4. Summary and Conclusion

Summary. Aiming at exploring more realistic sunspot simulations by extending the ideas introduced by Nordlund (2015) and examined in Jurčák et al. (2020), we have carried out a parameter study in MURaM sunspot simulations under the potential-field initial condition, and varying

- initial magnetic field strength, B_0 : 20, 40, 80, and 160 kG,
- magnetic flux content F_{Gauss} and opposing flux B_{opp} ,
- box width, and
- resolution (96/32 km versus 32/16 km).

We have found:

1. The penumbral extent increases systematically with B_0 , from no penumbra at 20 kG to long, slender filaments at 160 kG.
2. Runs with $F_{\text{Gauss}} > 10^{22}$ Mx develop unrealistically large umbral vertical fields, B_z .

3. The most realistic sunspots come from $B_0 = 160$ kG, $F_{\text{Gauss}} = 10^{22}$ Mx, which produce (1) maximum $B_z = 4.2 - 4.5$ kG (still larger than found in observations), and (2) a realistic profile of B_z and B_r with radius.
4. Closing the bottom boundary inside the spot trunk does not create a realistic sunspot.
5. Varying B_{opp} or the box width changes the background B_z outside the spot but does not significantly affect the internal spot structure or dynamics.
6. For $B_0 \leq 40$ kG, no Evershed flows develop, only in- and down-flows, little flux emergence.
7. For $B_0 = 80 - 160$ kG and low resolution (96/32 km), bi-directional flows as those found in observations of the early stages of penumbra formation are found during ongoing flux emergence.
8. High-resolution (32/16 km) runs produce both filaments with bi-directional flows and filaments with Evershed flows.

Conclusion. From this parameter study, we conclude that simulations initialised with potential-field conditions, sunspot fluxes on the order of 10^{22} Mx, and strong (160 kG) magnetic fields and open bottom boundary reproduce key aspects of the observed morphology and dynamics of sunspots during the early phases of penumbra formation (see, e.g. Schlichenmaier et al. 2010a; Jurčák et al. 2014): penumbral-like regions characterised by slender granulation of reduced intensity which, rather than exhibiting the classical radial velocities of the Evershed flow (Schlichenmaier & Schmidt 2000; Löhner-Böttcher & Schlichenmaier 2013), show bi-directional motions likely driven by flux emergence at the outskirts of the spot (García-Rivas et al. 2024). The results highlight the value of these simulations in investigating the initial stages of sunspot formation.

Comparison with failed simulations shows that, at least for low-resolution simulations with potential field top boundary conditions, we only get a realistic-looking sunspot with outwards flow in a sufficiently wide penumbra, while flux keeps emerging in the outer parts of the spot.³ We speculate that any low-density plasma in \cap -shaped magnetic field lines below the surface might be sufficient to drive flux emergence and create penumbrae as in our simulations.

However, observations suggest that an overlying canopy is required to form a stable penumbra with Evershed flows (Lindner et al. 2023; Chifu et al. 2025). Older simulations achieved this by forcing the field to be more inclined at the top boundary, such that the inclined field drives the Evershed flows. The presence of Evershed flows in some of the filaments of our high-resolution simulations, and their absence in the low-resolution simulations, indicates that insufficient resolution is an inhibiting factor for Evershed flows, consistent with preliminary reports by Rempel & Hotta (2025). We speculate that embedding the spot in a much larger (in all dimensions, above and below the photosphere) simulation box, including a small-scale dynamo run which allows a canopy to form naturally, might also force the field to be sufficiently inclined, so that Evershed flows might form even in low-resolution simulations, if the spot is placed in the right location.

Acknowledgements. We thank the anonymous reviewer for their valuable and insightful comments, which helped improve this manuscript. This work was supported by the Czech-German common grant, funded by the Czech Science

³ The causes behind the flux emergence in our simulations relate to the unphysical entropy enhancement during the initial transient and are beyond the scope of this article.

Foundation under project 23-07633K and by the Deutsche Forschungsgemeinschaft under project BE 5771/3-1 (eBer-23-13412), and the institutional support ASU:67985815 of the Czech Academy of Sciences. Most of the simulations leading to the results obtained were run on Piz Daint at the Swiss National Supercomputing Centre, Switzerland, financed through the ACCESS programme of the SOLARNET project, which has received funding from the European Union Horizon 2020 research and innovation programme under grant agreement no 824135. For the older simulations, we would like to thank Matthias Rempel for providing us with their data and acknowledge the high-performance computing support from Cheyenne (doi:10.5065/D6RX99HX) provided by the NCS NCAR's Computational and Information Systems Laboratory, sponsored by the National Science Foundation. This research has made use of NASA's Astrophysics Data System Bibliographic Services.

References

Beck, C. 2008, *A&A*, 480, 825
 Bellot Rubio, L. R., Balthasar, H., & Collados, M. 2004, *A&A*, 427, 319
 Bhatia, T. S., Panja, M., Cameron, R. H., & Solanki, S. K. 2025, *A&A*, 693, A264
 Borrero, J. M. & Ichimoto, K. 2011, *Living Reviews in Solar Physics*, 8, 4
 Borrero, J. M., Solanki, S. K., Bellot Rubio, L. R., Lagg, A., & Mathew, S. K. 2004, *A&A*, 422, 1093
 Chen, F., Rempel, M., & Fan, Y. 2017, *ApJ*, 846, 149
 Cheung, C. M. M. 2006, PhD thesis, Georg August University of Gottingen, Germany
 Cheung, M. C. M., Rempel, M., Title, A. M., & Schüssler, M. 2010, *ApJ*, 720, 233
 Chifu, I., Bello González, N., & Jurčák, J. 2025, *A&A*, 699, A218
 Chowdhury, P., Kilcik, A., Saha, A., et al. 2024, *Sol. Phys.*, 299, 19
 García-Rivas, M., Jurčák, J., Bello González, N., et al. 2024, *A&A*, 686, A112
 Heinemann, T., Nordlund, Å., Scharmer, G. B., & Spruit, H. C. 2007, *ApJ*, 669, 1390
 Hotta, H. & Iijima, H. 2020, *MNRAS*, 494, 2523
 Jurčák, J., Bellot Rubio, L. R., & Sobotka, M. 2014, *A&A*, 564, A91
 Jurčák, J., Schmassmann, M., Rempel, M., Bello González, N., & Schlichenmaier, R. 2020, *A&A*, 638, A28
 Keppens, R. & Martinez Pillet, V. 1996, *A&A*, 316, 229
 Kiess, C., Rezaei, R., & Schmidt, W. 2014a, *A&A*, 565, A52
 Kiess, C., Rezaei, R., & Schmidt, W. 2014b, *A&A*, 565, A52
 Lindner, P., Kuckein, C., González Manrique, S. J., et al. 2023, *A&A*, 673, A64
 Löhner-Böttcher, J., & Schlichenmaier, R. 2013, *A&A*, 551, A105
 Ludwig, H.-G. 1992, PhD thesis, Christian-Albrechts-Universität zu Kiel
 Mathew, S. K., Lagg, A., Solanki, S. K., et al. 2003, *A&A*, 410, 695
 Nordlund, Å. 1982, *A&A*, 107, 1
 Nordlund, Å. 2015, Nordita Seminar on Sunspot Formation: Theory, Simulations and Observations
 Panja, M., Cameron, R., & Solanki, S. K. 2020, *ApJ*, 893, 113
 Panja, M., Cameron, R. H., & Solanki, S. K. 2021, *ApJ*, 907, 102
 Rempel, M. 2012, *ApJ*, 750, 62
 Rempel, M. 2014, *ApJ*, 789, 132
 Rempel, M. 2017, *ApJ*, 834, 10
 Rempel, M. & Hotta, H. 2025, in SDO 2025 Science Workshop, Boulder, Colorado, presentation nr. 13
 Rempel, M., Schüssler, M., Cameron, R. H., & Knölker, M. 2009a, *Science*, 325, 171
 Rempel, M., Schüssler, M., & Knölker, M. 2009b, *ApJ*, 691, 640
 Rezaei, R., Beck, C., & Schmidt, W. 2012, *A&A*, 541, A60
 Sánchez Cuberes, M., Puschmann, K. G., & Wiehr, E. 2005, *A&A*, 440, 345
 Scharmer, G. B., Nordlund, Å., & Heinemann, T. 2008, *ApJ*, 677, L149
 Scherrer, P. H., Schou, J., Bush, R. I., et al. 2012, *Sol. Phys.*, 275, 207
 Schlichenmaier, R., Bello González, N., Rezaei, R., & Waldmann, T. A. 2010a, *Astronomische Nachrichten*, 331, 563
 Schlichenmaier, R., González, N. B., & Rezaei, R. 2011, in Physics of Sun and Star Spots, ed. D. Prasad Choudhary & K. G. Strassmeier, Vol. 273, 134–140
 Schlichenmaier, R., Rezaei, R., Bello González, N., & Waldmann, T. A. 2010b, *A&A*, 512, L1
 Schlichenmaier, R. & Schmidt, W. 2000, *A&A*, 358, 1122
 Schmassmann, M., Bello González, N., Jurčák, J., & Schlichenmaier, R. 2025, *A&A*, in print [arXiv:2512.11160]
 Schmassmann, M., Rempel, M., Bello González, N., Schlichenmaier, R., & Jurčák, J. 2021, *A&A*, 656, A92
 Schmassmann, M., Schlichenmaier, R., & Bello González, N. 2018, *A&A*, 620, A104
 Spruit, H. C. 1981, in The Physics of Sunspots, ed. L. E. Cram & J. H. Thomas, 98–103
 Tiwari, S. K., van Noort, M., Lagg, A., & Solanki, S. K. 2013, *A&A*, 557, A25
 Vögler, A., Bruls, J. H. M. J., & Schüssler, M. 2004, *A&A*, 421, 741
 Westendorp Plaza, C., del Toro Iniesta, J. C., Ruiz Cobo, B., et al. 2001, *ApJ*, 547, 1130

Appendix A: Initial magnetic field configurations

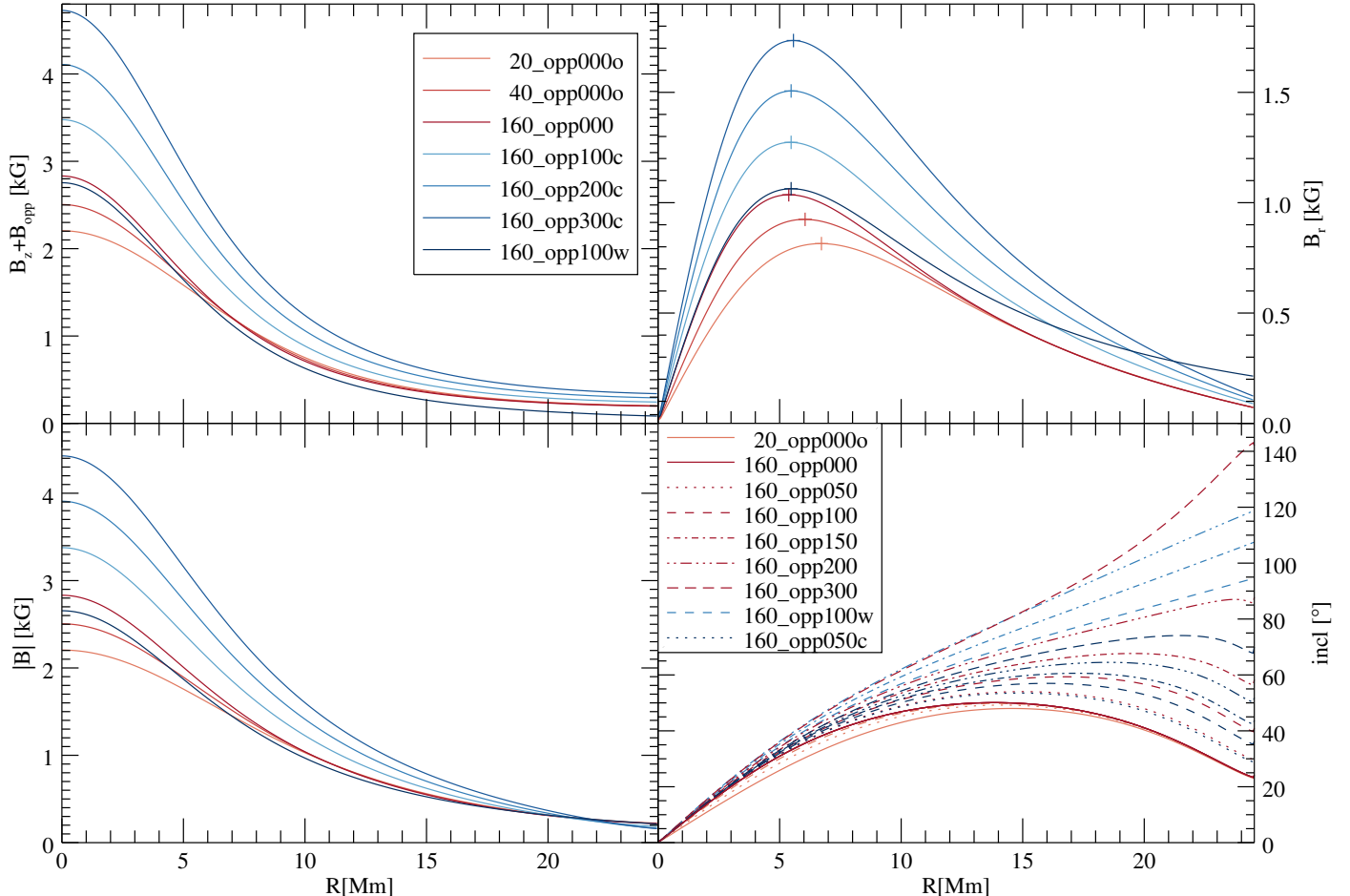


Fig. A.1. Initial magnetic field. The vertical field $B_z + B_{\text{opp}}$ (top left), radial field B_r (top right), total field $|B|$ (bottom left), and inclination to the surface normal γ . The legend in the top left panel shows the simulations plotted in the first three panels. The legend in the bottom right panel gives a selection of the simulations shown there, the rest is given in table A.1; for each line in that table (colour), the further right the column is (the higher B_0 or B_{opp} , the changing numbers in the run names), the higher the inclination.

Table A.1. Colours and line styles for simulations in bottom right panel of Fig. A.1, showing the inclination in the initial field

colour \ line style	—	...	--	---	— · ·	— —	comment
light red	20_opp000o	40_opp000o	80_opp000o				$B_0 < 160 \text{ kG}$
dark red	160_opp000?	160_opp050	160_opp100	160_opp150	160_opp200	160_opp300	$w = 98.304 \text{ Mm}$
light blue			160_opp100w	160_opp150w	160_opp200w		$w = 98.304 \text{ Mm}$
dark blue		160_opp050c	160_opp100c	160_opp150c	160_opp200c	160_opp300c	$F_{\text{Gauss}} > 10^{22} \text{ Mx}$

Figure A.1 shows the azimuthal averages of the initial magnetic field at the average height of the $\tau = 1$ iso-surface in the quiet Sun. The top two panels ($B_z + B_{\text{opp}}$ and B_r), show the initial conditions for all our simulations (except '80_opp000o' and 'alpha*'), because introducing a $B_{\text{opp}} \neq 0$ only offsets B_z uniformly, and does not affect B_r . In the bottom right panel, all simulations (except 'alpha*') are plotted. Colours and line-styles are described in Table A.1, where the '?' in '160_opp000?' is a wild-card, standing for any of 'o', 'ho', 'h', ' ', or 'b', since these simulations share the same initial conditions.

While this figure shows many details, primarily the following aspects are pertinent: 1) $F_{\text{Gauss}} > 10^{22} \text{ Mx}$ leads to strong B_z on the spot axis. 2) $w = 98.304 \text{ Mm}$ leads to the field being distributed over a wider box, resulting in a weaker B_z far from the spot axis and more extended B_r . 3) The inclinations in the initial conditions show a wide range of behaviour, in particular outside the spot.